A study of deformation and strain induced in bulk by the oxide layers formation on a Fe-Cr-Al alloy in high-temperature liquid Pb-Bi eutectic

M. P. Popovic[1*], K. Chen[2*], H. Shen[2, 3], C. V. Stan[3], D. L. Olmsted[4], N. Tamura[3], M. Asta[4], M. D. Abad[5] and P. Hosemann[1]

[1] Department of Nuclear Engineering, University of California, Berkeley, CA 94720, USA

[2] Center for Advancing Materials Performance from the Nanoscale (CAMP-Nano), State Key Laboratory for Mechanical Behavior of Materials, Xi'an Jiaotong University, Xi'an, Shaanxi 710049, China

[3] Advanced Light Source, Lawrence Berkeley National Laboratory, Berkeley, CA 94720, USA

[4] Department of Materials Science and Engineering, University of California, Berkeley, CA 94720, USA

[5] Instituto Quimico de Sarria, School of Engineering, University Ramon Llull, Barcelona, Spain

Abstract

At elevated temperatures, heavy liquid metals and their alloys are known to create a highly corrosive environment that causes irreversible degradation of most iron-based materials. It has been found that an appropriate concentration of oxygen in the liquid alloy can significantly reduce this issue by creating a passivating oxide scale that controls diffusion, especially if Al is present in Fe-based materials (by Al-oxide formation). However, the increase of the temperature and of oxygen content in liquid phase leads to the increase of oxygen diffusion into bulk, and to promotion of the internal Al oxidation. This can cause a strain in bulk near the oxide layer, due either to mismatch between the thermal expansion coefficients of the oxides and bulk material, or to misfit of the crystal lattices (bulk vs. oxides). This work investigates the strain induced into proximal bulk of a Fe-Cr-Al alloy by oxide layers formation in liquid lead-bismuth eutectic

* Corresponding authors: popovic@berkeley.edu, kchenlbl@gmail.com

utilizing synchrotron X-ray Laue microdiffraction. It is found that internal oxidation is the most likely cause for the strain in the metal rather than thermal expansion mismatch as a two-layer problem.

1. Introduction

Lead-bismuth eutectic (LBE: 44.5 wt% Pb, 55.5 wt% Bi) is an attractive alloy for use as a fluid in heat storage and transport applications in nuclear and solar power generating systems [1-4], due to its reduced melting point (123.5 ^{o}C), low viscosity, low reactivity, high thermal conductivity and proper neutron yield [6-8]. In high power density systems, just as in nuclear power and concentrated solar power systems are, an efficient and nonreactive heat transfer fluid is an essential component. The limiting factors of thermal efficiency are the temperature at which heat enters the engine and temperature of the environment where the heat is exhausted. In order to achieve high thermal efficiency in these fluids, it is necessary to maintain the temperature difference in the system, between the 'cold leg' (heat uptake) and 'hot leg' (heat delivery), at the maximum possible. Since the minimum temperature in the system is limited by the melting point of LBE, it is necessary to increase the hot-leg temperature as much as possible. However, a major drawback in using liquid LBE at high temperatures elevation is the increasing solubility of many chemical elements [3, 11, 13-16] and the potential for liquid-metal-assisted corrosion (LME) of the structural materials in contact with LBE [5, 11-14]. Besides the above mentioned phenomena, applying stress to the unprotected solid metals exposed to liquid metals, the former may experience liquid metal embrittlement (LME), characterized by premature brittle failure, depending on various parameters [72, 73]. At lower and higher temperatures, LME is less of an issue, leading to a temperature interval ("ductility trough") wherein the material is susceptible to LME (typically in 300 – 450 C range, for ferritic and ferritic-martensitic alloys) [74-76]. These

issues can be mitigated or reduced by adding an appropriate amount of oxygen into liquid LBE and keeping control of the oxygen concentration in order to form a protective oxide layer or layers on or near the structural material surface [3, 17-19]. The oxidation of the elements from liquid and solid phase depends on temperature, oxygen concentration and chemical potential (Gibbs free energy change, ΔG) of oxidation. This is represented by the Ellingham diagram, which enables visualization of whether the oxidation of a particular element is thermodynamically possible or not at certain predefined conditions. This mechanism leads to the use of structural alloys which should contain strong oxide formers with stable and diffusion-limiting oxides.

A significant number of studies on the formation of oxide layers in LBE at temperatures above 450 ^{0}C have been performed on a variety of different steels, leading to theoretical models of oxide formation proposed [20-26]. Austenitic (Fe-Cr-Ni) steels cannot be used at temperatures > 550 ^{0}C because of the high solubility (S) of nickel in lead and bismuth at these temperatures ($\log S_{Ni} = 1.53 - 873/T$, for $673 < T < 1173$ K) [28]. Therefore ferritic, ferritic-martensitic (F/M) and oxide dispersion-strengthened (ODS) alloys are better candidates for such applications. It has been shown that the addition of aluminum to the Fe-based ferritic materials is beneficial in preventing corrosion attack and severe oxidation, by forming an Al-rich oxide layer [29-34]. A thin but adherent Al_2O_3 oxide layer provides an effective diffusion barrier for Fe, Cr, Pb and Bi and protect the steel from heavy liquid metal attack [33-35]. 4-7 wt% of Al in addition to 12.5-17 wt% Cr are found to be sufficient to form an alumina layer in ferritic Fe-Cr-Al alloys at 400-750 ^{o}C, while lower Al concentrations (as well as higher Al if there is $\leqslant$ 10 wt% Cr) lead to the formation of Fe- based spinel-type oxides, $Fe_{3-x-y}Cr_xAl_yO_4$, both in air and Pb/LBE [33, 34, 36]. Generally, the higher the Cr content present, the lower the Al content that is acceptable. Fe-Cr-Al

alloys display a so-called 'third element effect' (TEE), where Cr (having an oxygen affinity intermediate between those of Fe and Al) is supposed to induce a transition between the internal and external oxidation of Al on ternary alloys under lower Al levels than for binary Fe-Al alloys [37-39]. The grown alumina scales are transient polymorphs that gradually transform into stable alumina [40] implying a volumetric change of ~14% in transformation from γ-Al_2O_3 into α-Al_2O_3 [41]. Spinel oxides have low thermal conductivity, while magnetite (Fe_3O_4) is reported to tend to spall off [37, 42]. Spalling is reported also for Al_2O_3 protective scales [19, 33, 34, 36 and 43].

While the oxide layers themselves have been subject to numerous studies, the interaction between the oxide layer and the substrate alloy has received only limited attention. In case of high temperatures and higher oxygen concentrations in LBE, the diffusion of oxygen through the oxide layers and into the steel bulk can become significant and lead to internal oxidation of Al, particularly along the grain boundaries [44]. Strain generation in the oxide and in near-oxide bulk due to the mismatch between the crystal structures of the oxides in scale and of the bulk has been reported previously [45, 47]. This mismatch might be one of the reasons for the oxide scales failure (breaking, spalling) that leads to the uncontrolled material dissolution/loss. The influence of Cr content on the microstructure and interfacial adhesion of the oxide scale formed on steel alloys has been investigated [46] and it was found that the Cr-oxide layers survived up to 5% of the tensile strain, while the Cr content in oxide phase determines the adhesion strength of the scales. In addition, the thermal expansion coefficient mismatch between the oxides and the bulk might also contribute to the oxide spalling, in cooling at the end of heat transfer systems operation. Abad et al. investigated the binding strength between the oxide layers and metals by using small scale mechanical testing [42], but the strain in the metal upon cooling of oxidized

samples has not been evaluated. It may be responsible for breaking and spalling of oxide layers especially if thermal cycling (as in solar thermal applications) is considered [47-51]. Therefore, the crystal lattice misfit and the thermal expansion mismatch are complimentary features and can both contribute to the oxide scales failure. The intention of this study is to examine what mechanism might be the most dominant one in Fe-Cr-Al alloy, at the upper limit ("hot-leg") temperature of 800^{0}C. In the study, we evaluate the micro-strain and distribution of plastic deformation near the steel-oxide interface in a Fe-Cr-Al alloy by using synchrotron X-ray Laue microdiffraction (μXRD). This proved to be an efficient method for correlation of mechanical properties with local structure at micron scale [52-57].

2. Experimental

Alkrothal 720 (ALK), a ferritic iron-chromium-aluminum BCC alloy with high thermal and corrosion resistivity (lattice constant a = (2.866 ± 0.001) Å, and composition provided by the vendor (Sandvik) [71]: 12-14% Cr, 4.0% Al (nominal), 0.7% Mn (max.), 0.7% Si (max.), 0.25% Ti (max.), and 0.08% C (max.) by weight with the balance of Fe), was exposed to liquid LBE at (800 ±5) ^{0}C for (360 ±1) h in an in-house designed experimental setup in controlled oxygen atmosphere (~ (5.0 ± 0.5)×10^{-6} wt% oxygen in LBE, monitored by oxygen sensor), according to the test procedure described in previous work [19]. 800^{0}C was chosen as a projected upper-limit operational temperature (beyond the temperatures previously used in LBE studies) for achieving better thermal efficiency. 360 h is a half month (15 days) period, which was the maximum permitted by the extent of the entire test matrix used in our wider research. Oxygen concentration was chosen based on the Ellingham's diagram as a near-minimum value needed for Fe-, Cr- and Al- oxides formation while disabling oxidation of lead and bismuth. After the corrosion test, the sample was extracted from the liquid LBE (before solidification, at ~ 200 ^{o}C) while the test

system was cooling down to room temperature, mounted in epoxy resin and subsequently cut in cross-section in the epoxy after ~ 12 h (time for epoxy resin to harden). This procedure ensures that the oxide layers are preserved as they appear on the material. Cross-sectioned ALK sample was polished first down to 1200 grid by SiC paper followed by diamond suspension and 0.3 μm Al_2O_3 solution (given in detail in ref. [19]), then analyzed by Quanta 3D field emission gun (FEG) scanning electron microscope equipped with energy-dispersive X-ray spectrometer "Oxford instruments", ~ 15 hours after the end of the corrosion test.

Laue μXRD measurements were carried out ~ 23 h after the end of corrosion test, on Beamline 12.3.2 at the Advanced Light Source (ALS), Lawrence Berkeley National Laboratory [55]. A schematic of the Laue diffraction setup and the details are given in Ref. [56]. The sample was mounted on a high resolution x–y scanning stage with its polished cross-section facing up, at a 45° tilt angle relative to the incident X-ray beam. Prior to XRD scan, a fast X-ray fluorescence (XRF) scan was conducted using a Si drift detector to position the sample edge (to ensure that all diffraction scans cover the desired region) and detect the expected elements in the scanned region. A polychromatic X-ray beam (5–24 keV) was focused by a pair of Kirkpatrick–Baez (KB) mirrors to ~ 1 × 1 μm^2 at the full width half maximum of the beam. Measurements were conducted in the near-surface region that includes the oxide layer over a 100 × 50 μm^2 area, as shown in Figure 1a.

The diffraction scanning step size was 1 μm, and a Laue pattern was recorded at each step with 1 s exposure time using an area DECTRIS Pilatus 1M detector which was placed about 140 mm away from the X-ray focal point at 90° with respect to the incoming beam. The diffraction geometrical parameters including sample-to-detector distance, center channel position and tilt of the detector were calibrated by indexing a Laue diffraction pattern taken from a strain free sharp

diffraction pattern within the sample far from the interface of the specimen using an in-house developed software XMAS [57]. Then all the 5000 recorded Laue patterns were automatically indexed using XMAS to obtain the crystal orientation and lattice strain at each scanning position. This technique provides high resolution of both crystal orientation (0.01°) [58] and of deviatoric strain (~10^{-4}) [59], while the defect type and density distribution in the scan area can also be revealed from the shape of the diffraction peaks [60-61].

3. Results

Scanning electron microscopy (SEM) with energy-dispersive X-ray spectrometry (EDS) analysis revealed a complex, multi-layer structure of oxide scale (Figure 1 b-c) of a total thickness of 10-15 μm. Closest to the steel, a layer consisting of mostly Al-oxide (~5 μm) has been detected, followed by a Fe-Cr(-Al)-oxide (~6 μm), and then another one mostly-Al-oxide layer (~4 μm) closest (next) to the LBE (Fig. 1c). Localized discontinuities in the inner Al-oxide layer have been found, as well as the traces of Pb and Bi within the outer Al-oxide (the latter contributing to the difference in contrast observed in the SEM images, as in Fig. 1b).

Two maps of 50×100 pixels are generated from the μXRD patterns, as described elsewhere [55]: recorded intensity map (RIM) and filtered intensity map (FIM). In the RIM, four different zones are visible (Figure 2a): besides the epoxy-holder region which is the lowest-intensity one, the next lowest intensity one is the low-ordered (phase-transformed) region that corresponds to the oxide phase grown atop the steel surface (10-15 μm, in the center), while to the right is the zone of Pb-Bi residues (~ 25 μm) above the oxide scale (with structural elements dissolved in it) and furthest one is zone of epoxy, while to the left is the best-ordered (the brightest zone), the bulk steel crystal. The FIM image (Figure 2b) is obtained by adding a filter of four times of the average intensity of each pattern to qualitatively map the defect density and

grain boundaries, so the bulk Fe-Cr-Al steel substrate, which is almost a single crystal, is visible, while the rest (phase-transformed zones of oxide and solidified Pb-Bi residues) is mostly dark on the image, with only traces from LBE residues still remaining a bit lighter in the dark background. Comparing the two intensity maps as shown in Figures 2a and 2b (FIM and RIM), allows to clearly distinguish between the steel, the oxide and the LBE zones (phases).

After filtering (≥ 6 peaks indexed), the crystal orientation at all scanning positions of the remained area relative to the arbitrarily chosen [001] direction has been obtained. A slight variation (deviation) of up to 0.2º in orientation of the segments of the steel crystal has been found close to the interface (with a minimum detectable change of 0.01º, being the error magnitude), so the orientation map is represented in a narrow range of 26.7º - 27.0º (Figure 2c), with a complementary misorientation map (Figure 2d) obtained by comparing the orientation matrix of each adjacent pair of scanning pixels, following the method introduced elsewhere [62]. This uncovers the fine orientation differences that represent possible plastic deformation and defect formation.

The peak width is defined as the average full width at half maximum (FWHM), in the unit of degrees, of all indexed reflections in each Laue diffraction pattern. The peak width increases and becomes significantly broadened in the region close to the metal/oxide interface within the steel, concurrent with a decrease in observed peak intensity. The average peak width evolution has been tracked along three lines parallel to the longer edge of XRD scan spot, i.e. varying the X-coordinate (red, black and yellow lines in Figure 3a) and plotted in Figure 3b. These line scans reveal a monotonic, uniform broadening (peak width increase).

In order to reveal the mechanism that produces peak broadening, quantitative peak shape analysis is performed on the $(0\bar{1}3)$ peak, which was chosen because it was the most intense peak

observed. Peak width has been measured by fitting the intensity with Lorentzian distribution function, so that the width was determined with a precision of ~ 0.1 pixels. The FWHM of the peak in chosen spots increases as we go from the bulk towards the steel-oxide interface (Figures 3c-e). There is a slight change in crystal orientation detected near the interface (crystal misorientation) that comes after the onset of increase in peak width as we move from the deep towards the proximal bulk zone. This indicates a subgrains generation in a tiny zone of orientation changes, narrower than the zone of plastic deformation (peak broadening). The anisotropic broadening indicates the existence of plastic deformation achieved by the geometrically necessary dislocations (GNDs), i.e. the dislocations exceeding in one sign (also called unpaired or polar dislocations) which occur due to the non-uniform plastic deformation accompanied by plastic strain gradients in material [70]. For simplicity, a typical $(0\bar{1}3)$ peak has been chosen and analyzed from the three co-linear spots (along the same line, parallel to the X-coordinate: see red dots b - d on Figure 4a) and distanced 35 µm, 15 µm and 7 µm respectively (on the X-axis) from the oxide interface. The diffraction peak evolution has been monitored and peak shape (dimensions) in the X-Y plane/projection has been analyzed (Figure 4, b - d). While moving from alloy bulk towards the steel-oxide interface (along X-axis), there is a peak streaking in more than one direction detected, which indicates the activation of more than one dislocation slip systems. The tiny sharp peaks next to the main peak (circled, to the right, on Figure 4d) appear with every Fe peak in the selected pattern, indicating the appearance of a well-crystallized subgrain with slight rotation from the original matrix. However, it is not present in every pattern along the boundary zone. This suggests that the boundary is inhomogeneous, which indicates an intermittent protrusion of oxide phase into the bulk (in a form of internal oxidation).

Diffraction peak broadening is correlated to the defect density in a specimen according to Barabash et al. [63] and Maaβ et al. [64]. Streaking of Laue diffraction peaks can be linked to the density of GNDs. For the crystal lattice parameter of BCC iron a = (2.866 ± 0.001) Å, the Burgers vector is $b = \frac{1}{2} \cdot \langle 111 \rangle = a \cdot \frac{\sqrt{3}}{2} \approx 2.4825(9)$ Å , and the error is obtained as Δb = Δa·(b/a). Dislocation density (ρ_D) is calculated from the Cahn-Nye relation [65] as $\rho_D = 1/(R \cdot b)$. Here, 1/R is obtained as the lattice misorientation (in radians) per size of the scanned surface element (which is 1 μm, same in both X and Y directions), i.e. as the angular difference in crystal orientation between the two neighboring scanned surface elements, having the unit of rad/μm. Therefore, the dislocation density map is obtained from the orientation map. The error (uncertainty) of 1/R values corresponds to the misorientation gradient that is 0.01°/μm. The maximum GND density reaches the values of ~ 2×10^9 cm^{-2} (Figure 5). The dislocation density is significantly higher (at least 10 times) at some spots in the proximity of steel-oxide interface (≤ 10 μm depth from the interface), compared to the values in the deep bulk zone, and stays in a good correlation with the peak broadening zone (Figure 3a).

The strain tensor has been calculated using the formalism described in [66]. The principal strain direction is calculated as the eigenvector of the deviatoric strain tensor, i.e. the three eigenvectors and eigenvalues associated with the second order deviatoric strain tensor have been calculated [67]. The magnitude of the eigenvector is the corresponding eigenvalue (where the magnitudes of the eigenvectors are unified). Maximal and minimal magnitude vectors are plotted as the direction arrays of maximum and minimum compression in Figure 6 a-b, based on [68-69]. Because of the nature of deviatoric strain, the minimum of three eigenvalues is negative, while the maximum is positive, indicating compression and tension, respectively.

4. Discussion

In order to determine the reason behind the observed peak broadening, the diffraction patterns along one transect on the map (Figure 4a) have been analyzed in greater depth. In this region, peak broadening of the $(0\bar{1}3)$ peak derives from striking of the peak (Figure 4 b - d). Along this transect, only one dislocation direction is seen in the deep bulk. The increase in strain coincides with onset of a second activated dislocation system, indicated by the beginning of second peak streaking directions (Figure 4c). A third dislocation direction appears in the zone of large strain and maximum peak broadening, with side peaks arising, which indicates subgrain formation (Figure 4d). A plateau, shown in Figure 3b, is achieved once additional slip systems are activated, and after this system comes to saturation, the further dislocation increase leads to further broadening (i.e. peak width increase). For instance, at least 3 subgrains with similar but distinct orientations were indexed within one of the measurement spots located in the near-surface bulk zone. The misorientation between the two neighboring grains has been found to be about 21.6º, with the rotation axis roughly along the [011] axis of the first one of them. The orientation of the third one is found to be even closer to the orientation of the first one (with a tiny misorientation of only 1.1º between them), while the rotation axis is along the $[10\bar{1}]$ direction of the first one. The first and third grain come from the same initial grain (the third one being a subgrain of the first one, with almost identical orientation), while the second one is an entirely newly-formed grain. A change in crystal orientation (Figure 2c) arises there where the subgrain occurs, and coincides with the end of peak width plateau, i.e. the onset of further peak broadening (Figure 3 a-b). This may be achieved when the dislocation density limit (maximum) is reached in one slip system and an additional slip system is activated, as indicated by additional peak striking observed in Figure 4 c-d. Peak broadening is caused by plastic deformation that

subsequently induces subgrain formation near the surface. The appearance of subgrains with orientations that do not match the bulk steel may be interpreted as parts of the bulk transformation due to interpenetration of the oxide and bulk steel layers. This means that the near-interface bulk area is not entirely a single crystal.

In order to exclude the possible contribution of polishing to plastic deformation, an additional μXRD scan was performed on a second sample of the same material, polished but not treated in LBE. After polishing, but before annealing, the sample consists of smaller-size grains. μXRD scanning showed there is no significant contribution from polishing: even if there was any strain induced by polishing, the annealing effect in the beginning of exposure to LBE eliminates that strain. Besides that, maximum peak width values are only 1/3 of maximum values after exposure to 800 ºC LBE, even if there were no reduction due to the annealing (Figures 7 a-b).

The experimental data suggest a significant plastic strain in the ALK sample to about a 10-15 μm depth from the interface with the oxide layer, which implies a substantial source of deformation other than the expected effects occurring due to oxidation at the ALK/LBE initial interface. We considered two possible hypotheses that may explain these findings. One hypothesis is based on the internal oxidation within the metal, in the region near the oxide/metal interface. Internal oxidation is observed in bcc-Fe alloys containing Al and Cr [44], and so Al and Cr would be the candidates for oxidation, with Al → Al_2O_3 being the thermodynamically most favorable phase. We calculated the amount of strain that could be produced by oxidation of the available Al, and estimated the depth to which such oxidation could occur based on diffusion from the interface. The partial molar volumes of Al and Cr in ALK were computed using the Thermo-Calc TCFE7 database [27]. We assumed a Fe-Cr-Al composition of 83 : 13 : 4 wt%,

kept at 800 °C for 360 hours. The grain size was assumed to be large enough that only bulk diffusion of oxygen was relevant, i.e., neglecting grain boundary diffusion. Oxygen at the initial ALK/LBE interface was assumed to be in local equilibrium with LBE, which contained 5×10^{-6} wt% O based on our oxygen sensor reading. Another issue with this assumptions is that if a passivating alumina layer formed, the oxygen at the interface would no longer be expected to be in equilibrium with the LBE. Bulk diffusion of O was based on data for pure Fe, and at 800°C it was taken to be $D_O = 3.2 \times 10^{-8}$ m^2/s [44]. The rate of the oxidation reaction was assumed to be fast enough that diffusion of O was the limiting factor. Diffusion of Al was ignored since the diffusion rate of Al in Fe is much slower than that of O in Fe. Volumes and thermal expansion coefficients of Al_2O_3 [9] and Cr_2O_3 [10] were taken from literature data. If all of the locally available Al were oxidized, we found that the volume increase of the ALK would be 4.5%. The equivalent linear strain would be 1.5%, already quite large. Cr is more abundant in ALK, and has a somewhat larger volume increase on oxidation. If all the locally available Cr were oxidized the volume increase of the sample would be ~ 20%. Clearly, internal oxidation could lead to substantial plastic strain.

We calculated the potential depth of oxidation, assuming complete oxidation of Al only, and that at each point in time, all Al to a depth x (t) is oxidized, while none of the Al beyond is. We assumed the O concentration profile to be linear, equal to the fixed value at the interface, and zero at x (t). We accounted only for the oxygen transport required to oxidize the Al. The oxygen transport to maintain the linear concentration profile is much smaller, and was ignored. Setting the infinitesimal amount of O required to oxidize Al over a depth dx and area A with the amount transported over a time period dt gives an integral equation for x(t),

$$\frac{3}{2}c_*^{Al}Adx = AD\frac{c_*^{O}}{x}dt \tag{4.1}$$

$$xdx = \frac{2}{3}\frac{c_*^{O}}{c_*^{Al}}Ddt = \frac{2}{3}\frac{c_0^{O}}{c_0^{Al}}Ddt \tag{4.2}$$

Solving this gives the result:

$$x^2 = \frac{4}{3}\frac{c_0^{O}}{c_0^{Al}}Dt. \tag{4.3}$$

Here D is the diffusion coefficient for O, c_0^O is the atomic fraction of oxygen in the ALK at the interface, c_0^{Al} is the atomic fraction of Al in the ALK (before oxidation), $c_*^{O} = c_0^{O}\rho$ is the O atoms per unit volume in ALK at the interface, $c_*^{Al} = c_0^{Al}\rho$ is the Al atoms per unit volume, and ρ is the total atoms per unit volume of ALK. Substituting in the assumed values, at t = 360 h, x = 39 µm. This suggests that internal oxidation is a plausible candidate for the source of plastic strain that reaches 10-15 µm deep into the ALK. Al-oxide growth/formation may cause the striking and splitting of the grain structure in the near-surface bulk zone, by a plate (wall) formation, might be illustrated as 'driving a wedge into wood'.

The other hypothesis is that strain is induced by the temperature change (cooling) at the end of the static corrosion tests in LBE. The strain was calculated for ALK in LBE at 800ºC, supposing that the only oxides on the steel surface are Al_2O_3 and Fe_3O_4 (as the most dominant oxide species determined elsewhere [19]). The thermal expansion coefficient is temperature-dependent and for the three materials taken into account here (alumina, magnetite, and ALK steel) it is represented by a sigmoidal function [10] as a function of temperature. The strain in each material in the defined temperature range is given by:

$$\varepsilon = \int_{298K}^{1073K} \alpha(T)dT \tag{4.4}$$

where $\alpha(T)$ is the linear thermal expansion coefficient. The integral has been solved geometrically, as the calculated surface below the sigmoidal function. The calculated strain values for Al_2O_3, Fe_3O_4 and ALK steel in the defined temperature range (25^0C - 800^0C) are:

$$\varepsilon_{Al2O3} = 775 \cdot 8.4 \cdot 10^{-6} = 0.65\ \% \quad (4.5)$$

$$\varepsilon_{ALK} = 775 \cdot 14.2 \cdot 10^{-6} = 1.1\ \% \quad (4.6)$$

$$\varepsilon_{Fe3O4} = 775 \cdot 16.4 \cdot 10^{-6} = 1.3\ \% \quad (4.7)$$

We get a rough assessment of the resulting strain on/near the bulk-oxide interface as a consequence of thermal expansion: If Fe_3O_4 is the only oxide in the scale atop the steel surface, $\varepsilon_{Fe_3O_4} > \varepsilon_{ALK}$, and hence the resulting strain is:

$$\varepsilon_{Fe_3O_4} - \varepsilon_{ALK} = 2.2 \cdot 775 \cdot 10^{-6} = 0.17\ \% \quad (4.8)$$

However, if Al_2O_3 is the only oxide in the scale, we have $\varepsilon_{Al_2O_3} < \varepsilon_{ALK}$, so the resulting strain is:

$$\varepsilon_{Al_2O_3} - \varepsilon_{ALK} = -5.8 \cdot 775 \cdot 10^{-6} = -0.45\ \% \quad (4.9)$$

A positive value means that there is a tension in the oxide and compression in the bulk, and vice versa. Evidently, the contribution from the thermal expansion mismatch is not negligible, but the values are far below our measurements and the computed values when using the internal oxidation assumption. However, in all likelihood the strain found may be a combination of both internal oxidation and thermal expansion. In case of mixed oxide, or multi-layer scale (as it is the real case, at least in this study), the contribution of resulting strains, $A = (\varepsilon_{Fe_3O_4} - \varepsilon_{ALK})$ and $B = (\varepsilon_{Al_2O_3} - \varepsilon_{ALK})$ has to be weighted (keeping in mind the different signs of the values in Eq. 4.8 and 4.9) to calculate the total resulting strain, $\varepsilon_{tot.}$:

$$\varepsilon_{tot.} = x\mathrm{A} + (1\text{-}x)\mathrm{B}$$

where x is an assessed percentage of magnetite in scale, based on EDS analysis results.

5. Conclusions

1) Plastic deformation (dislocations induced) and sub-grain formation in the near-interface bulk zone were observed.

2) Dislocation density calculated from crystal mis-orientation correlates well with peak width and strain distribution, indicating that strain in the lattice mainly comes from plastic deformation

3) Grain refinement (rotation/tilting) of the bulk crystal structure (lattice) causes changing in crystal orientation in the near-interface region, and could be caused by internal oxidation, which subsequently induces strain due to the oxide and bulk crystal lattices misfit

4) We considered two possible origins of the strain induced in the bulk: one is the internal oxidation of aluminum through the diffusion of oxygen from LBE into bulk, while the other one is the thermal expansion mismatch between the oxide and the bulk. According to the results presented here, it is plausible that internal oxidation is the more dominant mechanism of strain induction.

Acknowledgements

This work is supported by the U.S. Department of Energy (DOE) SunShot program (Award No. DE-EE0005941), the National Natural Science Foundation of China (Grant No. 51671154 and 51405507), the National Key Research and Development Program of China (Grant No. 2016YFB0700404) and the National Basic Research Program of China ("973" Program) (Grant No. 2015CB057400). The authors thank Dr. Alan Bolind for some very helpful editing and improvement of the text, and Dr. Martin Kunz from the Experimental systems group at LBNL for technical assistance during the experiment. K.C. also

appreciates the supports from the open project of State Key Laboratory for Mechanical Behavior of Materials (Grant No. 20171907), and from the International Joint Laboratory for Micro/Nano Manufacturing and Measurement Technologies and the Collaborative Innovation Center of High-End Manufacturing Equipment. The ALS is supported by the Director, Office of Science, Office of Basic Energy Sciences, Materials Science Division, of the U.S. Department of Energy under Contract No. DE-AC02-05CH11231 at LBNL.

References

[1] OECD – NEA 7268, Handbook on Lead-bismuth Eutectic Alloy and Lead Properties, Materials Compatibility, Thermal- hydraulics and Technologies, 2015 Edition (https://www.oecd-nea.org/science/pubs/2015/7268-lead-bismuth-2015.pdf).

[2] C. Schroer, J. Konys, Physical Chemistry of Corrosion and Oxygen Control in Liquid Lead and Lead-Bismuth Eutectic, Forschungszentrum Karlsruhe (Wissenschaftliche Berichte FZKA 7364), 2007. (https://www.deutsche-digitale-bibliothek.de/binary/UXLSJBDAKUYFBCOB6OENDWQCLUZX4Y24/full/1.pdf)

[3] D. Frazer, E. Stergar, C. Cionea, P. Hosemann, Liquid Metal as a Heat Transport Fluid for Thermal Solar Power Applications, Energy Procedia 49 (2014), 627–636. http://www.sciencedirect.com/science/article/pii/S1876610214005220

[4] S. Khericha, E. Loewen, Nucl. Eng. Des. 241 (2011), Lead Coolant Test Facility—Design concept and requirements, 3008–3016. http://www.sciencedirect.com/science/article/pii/S0029549311004869

[5] K. L. Murty, I. Charit, J. Nucl. Mater. 383 (2008), Structural materials for Gen-IV nuclear reactors: challenges and opportunities, 189–195. http://www.sciencedirect.com/science/article/pii/S0022311508004960

[6] H. Aït Abderrahim, P. Baeten, D. De Bruyn, J. Heyse, P. Schuurmans, J. Wagemans, MYRRHA, a Multipurpose hybrid research reactor for high-energy applications, Nucl. Phys. News 20 (2010) 24–28. http://www.tandfonline.com/doi/abs/10.1080/10506890903178913

[7] J. Wallenius, ELECTRA-FCC: a centre for Generation IV system research and training, In: ELECTRA workshop presentations, Stockholm, Sweden 2012, KTH.

[8] M. Wohlmuther, W. Wagner, PIE preparation of the MEGAPIE target, J. Nucl. Mater. 431 (2012), 10-15. http://www.sciencedirect.com/science/article/pii/S0022311511009767

[9] G.K. White, M.L. Minges, Thermophysical properties of some key solids: An update, Int. J. Thermophys., 18 (1997) 1269-1327.

[10] Subvolume D 'Non-Tetrahedrally Bonded Binary Compounds II' of Volume 41 'Semiconductors' of Landolt-Börnstein - Group III Condensed Matter, Springer, Berlin, 2001.

[11] J. Zhang, N. Li, Review of the studies on fundamental issues in LBE corrosion, J. Nucl. Mater. 373 (2008), 351–377. http://www.sciencedirect.com/science/article/pii/S0022311507008422

[12] A.L. Johnson, D. Parsons, J. Manzerova, D. L Perry, D. Koury, B. Hosterman, J.W. Farley, Specotrscopic and microscopic investigation of the corrosion of 316/316L stainless steel by lead-bismuth eutectic (LBE) at elevated temperatures: importance of surface preparation, J. Nucl. Mater. 328 (2004), 88–96. http://www.sciencedirect.com/science/article/pii/S0022311504001102

[13] P. Hosemann, D. Frazer, E. Stergar and K. Lambrinou, Twin boundary-accelerated ferritization of austenitic stainless steels in liquid lead–bismuth eutectic, Scr. Mater. 118 (2016), 37-40. http://www.sciencedirect.com/science/article/pii/S1359646216300732

[14] M. de Caro, K. Woloshun, F. Rubio, S.A. Maloy, P. Hosemann, Heavy Liquid Metal Corrosion of Structural Materials in Advanced Nuclear Systems, JOM 65 (2013) 1057–1066. https://link.springer.com/article/10.1007/s11837-013-0663-7

[15] J. Abella, A. Verdaguer, S. Colominas, K. Ginestar, L. Martinelli, Fundamental data: solubility of nickel and oxygen and diffusivity of iron and oxygen in molten LBE, J. Nucl. Mat. 415 (2011) 329–337. http://www.sciencedirect.com/science/article/pii/S0022311511003953

[16] J. Zhang, A review of steel corrosion by liquid lead and lead– bismuth, Corros. Sci. 51 (2009) 1207–1227. http://www.sciencedirect.com/science/article/pii/S0010938X09000936

[17] N. Li, Active control of oxygen in molten lead-bismuth eutectic systems to prevent steel corrosion and coolant contamination, J. Nucl. Mater. 300 (2002) 73-81 http://www.sciencedirect.com/science/article/pii/S0022311501007139

[18] J. Zhang, Oxygen control technology in applications of liquid lead and lead-bismuth systems for mitigating materials corrosion, J. Appl. Electrochem. 43 (2013), 755-771. https://link.springer.com/article/10.1007/s10800-013-0568-8

[19] C. Cionea, M. D. Abad, Y. Aussat, D. Frazer, A. J. Gubser, P. Hosemann, Oxide scale formation on 316L and FeCrAl steels exposed to oxygen controlled static LBE at temperatures up to 800 ºC, Sol. En. Mater. Sol. Cell. 144 (2016), 235-246.

[20] L. Martinelli, F. Balbaud-Célérier, G. Picard, G. Santarini, Oxidation mechanism of an Fe–9Cr–1Mo steel by liquid Pb–Bi eutectic alloy at 470 °C (Part III), Corros. Sci. (2008) 2549–2559.

http://www.sciencedirect.com/science/article/pii/S0010938X08002552

[21] L.Martinelli, F. Balbaud-Célérier, A. Terlain, S. Bosonnet, G. Picard, G. Santarini, Oxidation mechanism of an Fe–9Cr–1Mo steel by liquid Pb–Bi eutectic alloy at 470 °C (Part II),

Corros. Sci. 50 (2008) 2537–2548
http://www.sciencedirect.com/science/article/pii/S0010938X08002540

[22] L. Martinelli, F. Balbaud-Célérier, A. Terlain, S. Delpech, G. Santarini, J. Favergeon, G. Moulin, M. Tabarant, G. Picard, Oxidation mechanism of an Fe–9Cr–1Mo steel by liquid Pb–Bi eutectic alloy at 470 °C (Part I), Corros. Sci. 50 (2008) 2523–2536.
http://www.sciencedirect.com/science/article/pii/S0010938X08002539

[23] B. X. He, N. Li, M. Mineev, A Kinetic Model for Corrosion and Precipitation in Non-Isothermal LBE Flow Loop, J. Nucl. Mater. 297 (2001), 214-219.
http://www.sciencedirect.com/science/article/pii/S0022311501006031

[24] J. Zhang, P. Hosemann, S. Maloy, Models of liquid metal corrosion, J. Nucl. Mater. 404 (2010) 82–96. http://www.sciencedirect.com/science/article/pii/S0022311510002369

[25] J. Zhang, Long-Term Behaviors of Oxide Layer in Liquid Lead–Bismuth Eutectic (LBE), Part I: Model Development and Validation, Oxid. Met. 80 (2013), 669-685. https://link.springer.com/article/10.1007/s11085-013-9450-7

[26] J. Zhang, Long-Term Behaviors of Oxide Layer in Liquid Lead–Bismuth Eutectic (LBE), Part II: Model Application, Oxid. Met. 81 (2014), 597-615.
https://link.springer.com/article/10.1007/s11085-014-9469-4

[27] Thermo-Calc Software, TCFE7 thermodynamic database (for steels and Fe-based alloys)
http://www.thermocalc.com/media/10306/tcfe7_extended_info_2013-02-07.pdf

[28] T. B. Massalski, *Binary Alloys Phase Diagrams*, The Materials Information Society, Materials Park (1990).

[29] G. Müller, G. Schumacher, F. Zimmermann, Investigation on oxygen controlled liquid lead corrosion of surface treated steels, J. Nucl. Mater. 278 (2000), 85-95.
http://www.sciencedirect.com/science/article/pii/S0022311599002111

[30] V. Gorynin, G.P. Karzov, V.G. Markov, V.A. Yakovlev, Structural materials for atomic reactors with liquid metal heat-transfer agents in the form of lead or lead—Bismuth alloy, Met. Sci. Heat. Treat. 41 (1999), 384–388.
https://link.springer.com/article/10.1007%2FBF02469876?LI=true

[31] M. Kondo, M. Takahashi, Corrosion resistance of Si- and Al-rich steels in flowing lead–bismuth, J. Nucl. Mater. 356 (2006), 203–212.
http://www.sciencedirect.com/science/article/pii/S0022311506002613

[32] J. Lim, H. O. Nam, I. S. Hwang, J.-H. Kim, A study of early corrosion behaviors of FeCrAl alloys in liquid lead–bismuth eutectic environments, J. Nucl. Mater. 407 (2010), 205-210.
http://www.sciencedirect.com/science/article/pii/S0022311510005982

[33] A. Weisenburger, A. Jianu, S. Doyle, M. Bruns, R. Fetzer, A. Heinzel, M. Del Giacco, W. An, G. Müller, Oxide scales formed on Fe–Cr–Al-based model alloys exposed to oxygen containing molten lead, J. Nucl. Mater. 437 (2013), 282-292.
http://www.sciencedirect.com/science/article/pii/S0022311513004509

[34] M. Del Giacco, A. Weisenburger, A. Jianu, F. Lang, G. Mueller, Influence of composition and microstructure on the corrosion behavior of different Fe–Cr–Al alloys in molten LBE, J. Nucl. Mater. 421 (2012), 39-46.
http://www.sciencedirect.com/science/article/pii/S002231151101004X

[35] S. Takaya, T. Furukawa, M. Inoue, T. Fujisawa, T. Okuda, F. Abe, S. Ohnuki and A. Kimura, Corrosion resistance of Al-alloying high Cr–ODS steels in stagnant lead–bismuth, J.

Nucl. Mater. 398 (2010) 132–138.

http://www.sciencedirect.com/science/article/pii/S0022311509008319

[36] P. Tomaszewicz, G. R. Wallwork, The oxidation of high-purity iron-chromium-aluminum alloys at 800°C, Oxid. Met. 20 (1983), 75–109.

https://link.springer.com/article/10.1007%2FBF00662042?LI=true

[37] Z. G. Zhang, X. L. Zhang, L. Sheng, X. Teng, "The effect of the third element Cr on oxidation behavior of Fe-xCr-10Al (at.%) alloy at 900^0C", The Effect of the Third Element Cr on Oxidation Behavior of Fe-xCr-10Al (at.%) Alloys at 900 ^{o}C, Open Corr. J. 2 (2009) 37-44.

https://benthamopen.com/contents/pdf/TOCORRJ/TOCORRJ-2-37.pdf

[38] F. H. Stott, G. C. Wood and J. Stringer, "The influence of alloying elements on the development and maintenance of protective scales", Oxid. Met. 44 (1995), 113-145. https://link.springer.com/article/10.1007/BF01046725

[39] C. Wagner, Passivity and inhibition during the oxidation of metal at elevated temperatures, Corros. Sci. 5 (1965), 751-764.

http://www.sciencedirect.com/science/article/pii/S0010938X65800038

[40] D. Naumenko, W. J. Quadakkers, A. Galerie, Y. Wouters and S. Jourdain, Parameters affecting transient oxide formation on FeCrAl based foil and fiber materials, High Temp. 20 (3) (2003), 287–293. http://www.tandfonline.com/doi/abs/10.1179/mht.2003.034

[41] R. Prescott and M. J. Graham, The formation of aluminum oxide scales on high-temperature alloys, Oxid. Met. 38 (1992), 233–254. https://link.springer.com/article/10.1007/BF00666913

[42] M. D. Abad, S. Parker, D. Frazer, M. Rebello de Figueiredo, A. Lupinacci, K. Kikuchi and P. Hosemann, Evaluation of the Mechanical Properties of Naturally Grown Multilayered Oxides

Formed on HCM12A Using Small Scale Mechanical Testing, Oxid. Met. 84 (2015), 211-231. https://link.springer.com/article/10.1007/s11085-015-9551-6

[43] A. Weisenburger, A. Heinzel, G. Muller, H. Muscher, A. Rousanov, T91 cladding tubes with and without modified FeCrAlY coatings exposed in LBE at different flow, stress and temperature conditions, J. Nucl.Mat. 376 (2008) 274-81. http://www.sciencedirect.com/science/article/pii/S0022311508000664

[44] M. Auinger, V.C. Praig, B. Linder, H. Danninger, Grain boundary oxidation in iron-based alloys, investigated by ^{18}O enriched water vapour – The effect of mixed oxides in binary and ternary Fe–{Al, Cr, Mn, Si} systems, Corrosion Sci. 96 (2015) 133-143. http://www.sciencedirect.com/science/article/pii/S0010938X15001699

[45] P. Hosemann, P. Dickerson, R. Dickerson, N. Li, S. A. Maloy, Transmission electron microscopy (TEM) on oxide layers formed on D9 stainless steel in lead bismuth eutectic (LBE), Corros. Sci. 66 (2013) 196–202. http://www.sciencedirect.com/science/article/pii/S0010938X12004490

[46] C.-W. Yang, J.-H. Kim, R. E. Triambulo, Y.-H. Kang, J.-S. Lee, J.-W. Park, The mechanical property of the oxide scale on Fe–Cr alloy steels, J. Alloy. Compounds 549 (2013) 6-10. http://www.sciencedirect.com/science/article/pii/S0925838812016362

[47] V. K. Tolpygo, D. R. Clarke, Spalling failure of a-alumina films grown by oxidation: I. Dependence on cooling rate and metal thickness, Mat. Sci. Eng. A 278, 1-2 (2000) 142-150. http://www.sciencedirect.com/science/article/pii/S092150939900581X

[48] V. K. Tolpygo, D. R. Clarke, Spalling failure of a-alumina films grown by oxidation: II Decohesion nucleation and growth, Mat. Sci. Eng. A 278, 1-2 (2000) 151-161. http://www.sciencedirect.com/science/article/pii/S0921509399005821

[49] C. Zhu, X. Zhao, I. S. Molchan, G. E. Thompson, G. Liang, P. Xiao, Effect of cooling rate and substrate thickness on spallation of alumina scale on Fecralloy, Mat. Sci. Eng. A 528 (2011) 8687-8693. http://www.sciencedirect.com/science/article/pii/S0921509311009294

[50] S. Wang, C. M. Harvey, B. Wang, Room temperature spallation of α-alumina films grown by oxidation, Eng. Fract. Mech. 178 (2017) 401-415. http://www.sciencedirect.com/science/article/pii/S0013794417302448

[51] C. Zhu, X. Zhao, Y. Chen, Y. Zhao, P. Xiao, I. S. Molchan, G. E. Thompson, Spallation Behaviour of Alumina Scale Formed on FeCrAlY Alloy After Isothermal Oxidation, Oxid. Met. 85 (2016) 391-408. https://link.springer.com/article/10.1007/s11085-015-9602-z

[52] M. Izumi, Y. Murakami, Y. Konishi, T. Manako, M. Kawasaki, and Y. Tokura, Structure characterization and magnetic properties of oxide superlattices, Phys. Rev. B **60** (1999) 1211. https://journals.aps.org/prb/abstract/10.1103/PhysRevB.60.1211

[53] J. H. Stout, D. A. Shores, J. G. Goedjen, M. E. Armacanqui, Stresses and cracking of oxide scales, Mat. Sci. Eng. A 120-121 (1989) 193-197. http://www.sciencedirect.com/science/article/pii/0921509389907399

[54] T. Homma and Y. Pyun, Proc. 3rd Japan Institute of Metals Int. Symp. on High Temperature Corrosion, Trans. Jpn. Inst. Met. Suppl., (1983), p. 161

[55] M. Kunz, N. Tamura, K. Chen, A. A. MacDowell, R. S. Celestre, M. M. Church, S. Fakra, E. E. Domning, J. M. Glossinger, J. L. Kirschman, G. Y. Morrison, D. W. Plate, B. V. Smith, T. Warwick, V. V. Yashchuk, H. A. Padmore, E. Ustundag, A dedicated superbend x-ray microdiffraction beamline for materials, geo-, and environmental sciences at the advanced light source, Rev. Sci. Instr. 80 (2009) 035108. https://doi.org/10.1063/1.3096295

[56] M. Kunz, K. Chen, N. Tamura, H.-R. Wenk, Evidence for residual elastic strain in deformed natural quartz, Am. Mineral. 94 (2009) 1059–1062. https://www.degruyter.com/view/j/ammin.2009.94.issue-7/am.2009.3216/am.2009.3216.xml

[57] N. Tamura, in: *Strain Dislocation Gradients from Diffraction. Spatially-Resolved Local Structure and Defects*, edited by R. Barabash and G. Ice, London, 2014 (pp. 125–155). https://books.google.com/books?hl=en&lr=&id=S9G6CgAAQBAJ&oi=fnd&pg=PR5&dq=N.+Tamura,+in:+Strain+Dislocation+Gradients+from+Diffraction.+Spatially-Resolved+Local+Structure+and+Defects,+edited+by+R.+Barabash+and+G.+Ice+(World+Scientific,+London,+2014),+pp.+125%E2%80%93155&ots=r5QVTQUMjG&sig=5igPgxH2YEtvtJiALiVieUpnalo#v=onepage&q&f=false

[58] K. Chen, N. Tamura, W. Tang, M. Kunz, Y. C. Chou, K. N. Tu, and Y. S. Lai, High precision thermal stress study on flip chips by synchrotron polychromatic x-ray microdiffraction, J. Appl. Phys. 107 (2010) 063502. http://aip.scitation.org/doi/abs/10.1063/1.3309750

[59] K. Chen, M. Kunz, N. Tamura, and H.-R. Wenk, Residual stress preserved in quartz from the San Andreas Fault Observatory at Depth, Geology 43 (2015), 219. https://pubs.geoscienceworld.org/geology/article-lookup/43/3/219

[60] A. Lupinacci, K. Chen, Y. Li, M. Kunz, Z. Jiao, G. S. Was, M. D. Abad, A. M. Minor, P. Hosemann, Characterization of ion beam irradiated 304 stainless steel utilizing nanoindentation and Laue microdiffraction, J. Nucl. Mater. 458 (2015), 70. http://www.sciencedirect.com/science/article/pii/S0022311514008411

[61] Dan Qian, Anfeng Zhang, Jianxue Zhu, Yao Li, Wenxin Zhu, Baolu Qi, Nobumichi Tamura, Dichen Li, Zhongxiao Song, Kai Chen, Hardness and microstructural inhomogeneity at

the epitaxial interface of laser 3D-printed Ni-based superalloy, Applied Physics Letters, 109, 101907, DOI: 10.1063/1.4962485, 2016. http://aip.scitation.org/doi/abs/10.1063/1.4962485

[62] Y. Li, L. Wan and K. Chen, A look-up table based approach to characterize crystal twinning for synchrotron X-ray Laue microdiffraction scans, J. Appl. Crystallogr., 48 (2015), 747-757 DOI: 10.1107/S1600576715004896 (http://scripts.iucr.org/cgi-bin/paper?nb5143)

[63] R. I. Barabash, G. E. Ice, Quantitative analysis of dislocation arrangements induced by electromigration in a passivated Al (0.5 wt% Cu)Al (0.5 wt% Cu) interconnect, J. Appl. Phys. 93 (2003) 5701. http://aip.scitation.org/doi/abs/10.1063/1.1563033

[64] R. Maaβ , S. Van Petegem, D. Grolimund, H. Van Swygenhoven, D. Kiener, G. Dehm, Crystal rotation in Cu single crystal micropillars: In situ Laue and electron backscatter diffraction, Appl. Phys. Lett. 92 (2008) 071905. http://aip.scitation.org/doi/pdf/10.1063/1.2884688

[65] B. C. Valek, N. Tamura, R. Spolenak, W. A. Caldwell, A. A. MacDowell, R. S. Celestre, H. A. Padmore, J. C. Bravman, B. W. Batterman, W. D. Nix, and J. R. Patel, Early stage of plastic deformation in thin films undergoing electromigration, J. Appl. Phys. 94 (2003), 3757. http://aip.scitation.org/doi/abs/10.1063/1.1600843

[66] J. S. Chung, G. E. Ice, Automated indexing for texture and strain measurement with broad-bandpass x-ray microbeams, J. Appl. Phys. 86 (1999), 5249-5255. http://aip.scitation.org/doi/abs/10.1063/1.371507

[67] G. Zhou, W. Zhu, H. Shen, Y. Li, A. Zhang, N. Tamura, K. Chen, Real-time microstructure imaging by Laue microdiffraction: A sample application in laser 3D printed Ni-based superalloys, Scientific Reports 6 (2016), 28144. https://www.ncbi.nlm.nih.gov/pmc/articles/PMC4908403/

[68] Y. Li, D. Qian, J. Xue, J. Wan, A. Zhang, N. Tamura, Z. Song, and K. Chen, A synchrotron study of defect and strain inhomogeneity in laser-assisted three-dimensionally-printed Ni-based superalloy, Appl. Phys. Lett. 107 (2015), 181902; doi: 10.1063/1.4934839 (http://aip.scitation.org/doi/10.1063/1.4934839)

[69] K. Chen, M. Kunz, Y. Li, E. Zepeda-Alarcon, M. Sintubin, and H.-R. Wenk, Compressional residual stress in Bastogne boudins revealed by synchrotron X-ray microdiffraction, Geophys. Res. Lett., 43 (2016) 6178–6185 (http://onlinelibrary.wiley.com/doi/10.1002/2016GL069236/abstract) doi:10.1002/2016GL069236

[70] G. E. Ice and R. I. Barabash, "White Beam Microdiffraction and Dislocations Gradients", *Dislocation in Solids*, Chapter 79, Vol. 13 (2007) 499-601. https://doi.org/10.1016/S1572-4859(07)80011-8

[71] Alkrothal 720 (ALK) datasheets: resistance heating wire and resistance wire (updated on 2017-01-19 at 11:22 AM), and strip (updated on 2017-12-06 at 10:51 AM). https://www.kanthal.com/en/products/material-datasheets/?query=Alkrothal&sort=

[72] B. Joseph, M. Picat, F. Barbier, "Liquid metal embrittlement: A state-of-the-art appraisal", Eur. Phys. J. AP 5 (1999) 19–31. https://doi.org/10.1051/epjap:1999108

[73] T. Sample, H. Kolbe, "Liquid metal embrittlement (LME) susceptibility of the 8–9% Cr martensitic steels F82H-mod., OPTIFER IVb and their simulated welded structures in liquid Pb–17Li", J. Nucl. Mater. 283–287 (2000) 1336–1340. https://doi.org/10.1016/S0022-3115(00)00097-0

[74] C. F. Old, "Liquid metal embrittlement of nuclear materials", J. Nucl. Mater. 92 (1980) 2–25. https://doi.org/10.1016/0022-3115(80)90136-1

[75] J. Van den Bosch, P. Hosemann, A. Almazouzi, S. A. Maloy, "Liquid metal embrittlement of silicon enriched steel for nuclear applications", J. Nucl. Mater. 398 (2010) 116–121. https://doi.org/10.1016/j.jnucmat.2009.10.020

[76] B. Long, Z. Tong, F. Gröschel, Y. Dai, "Liquid Pb–Bi embrittlement effects on the T91 steel after different heat treatments", J. Nucl. Mater. 377, 1 (2008) 219–224. https://doi.org/10.1016/j.jnucmat.2008.02.050

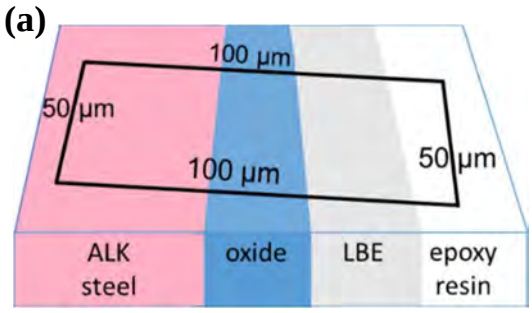

(c)

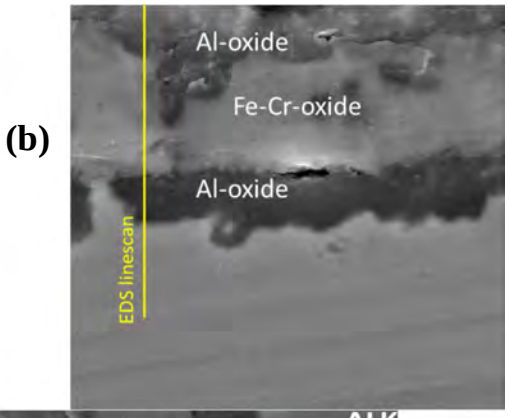

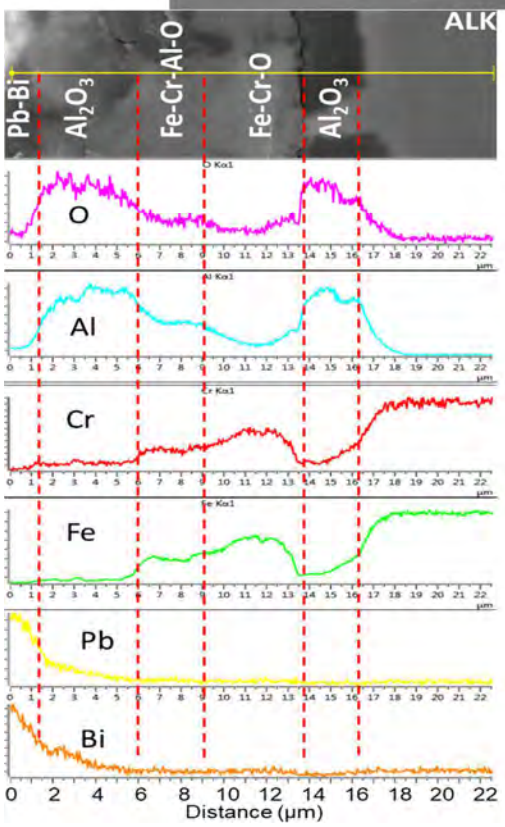

Figure 1. *(a) Laue-XRD analyzed spot (100 x 50 μm^2 rectangle) covering near-interface steel bulk, oxide layer grown on steel, and LBE residues over the oxide, as seen in perspective. The black box represents the XRD-scanned area; (b) SEM cross-section image of the oxide layers grown on ALK steel sample in exposure to Pb-Bi eutectic (LBE) at 800 ^oC; (c) EDS line scan of the oxide layers grown on tested ALK steel sample.*

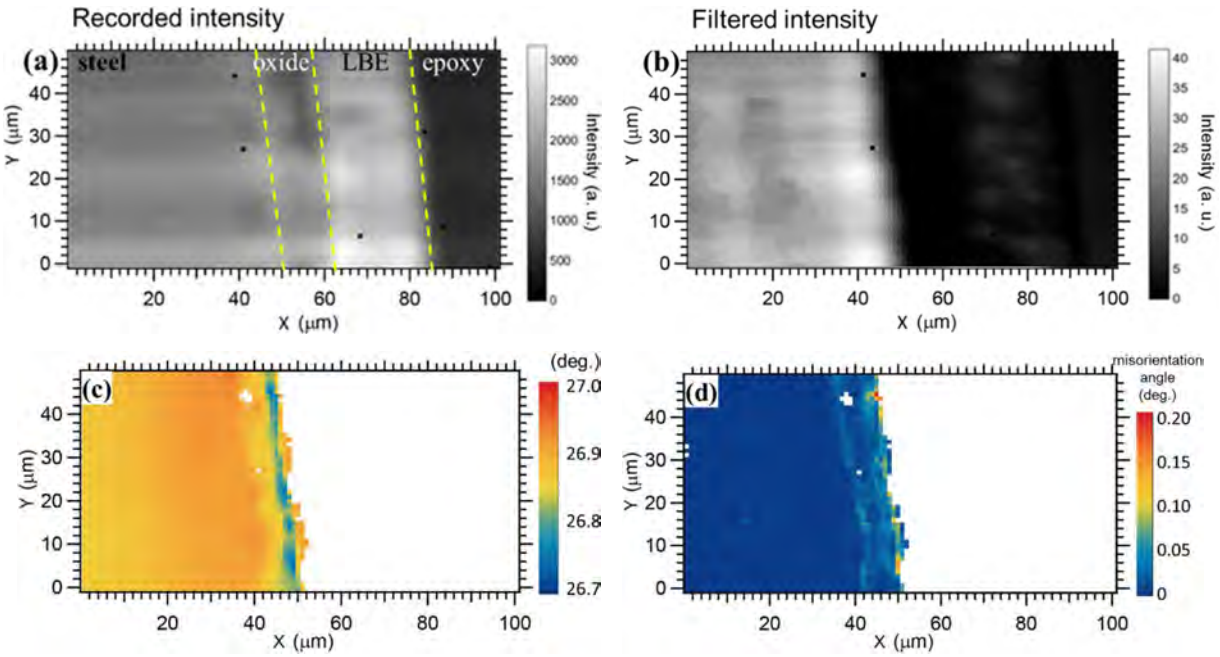

Figure 2. *(a) Recorded-intensity map (average intensity of the diffraction peaks); (b) Filtered-intensity map displaying spots with more than 6 peaks identifying BCC steel; (c) bulk crystal orientation map of [001] direction in a narrow angle range (26.7º-27.0º); (d) lattice mis-orientation map, obtained as the difference (subtraction) between the values of the neighboring pixels in image (c): two "belts" of a sudden drop/jump in orientation changes are visible near the bulk/oxide interface, indicating the formation of the sub-grains in that region.*

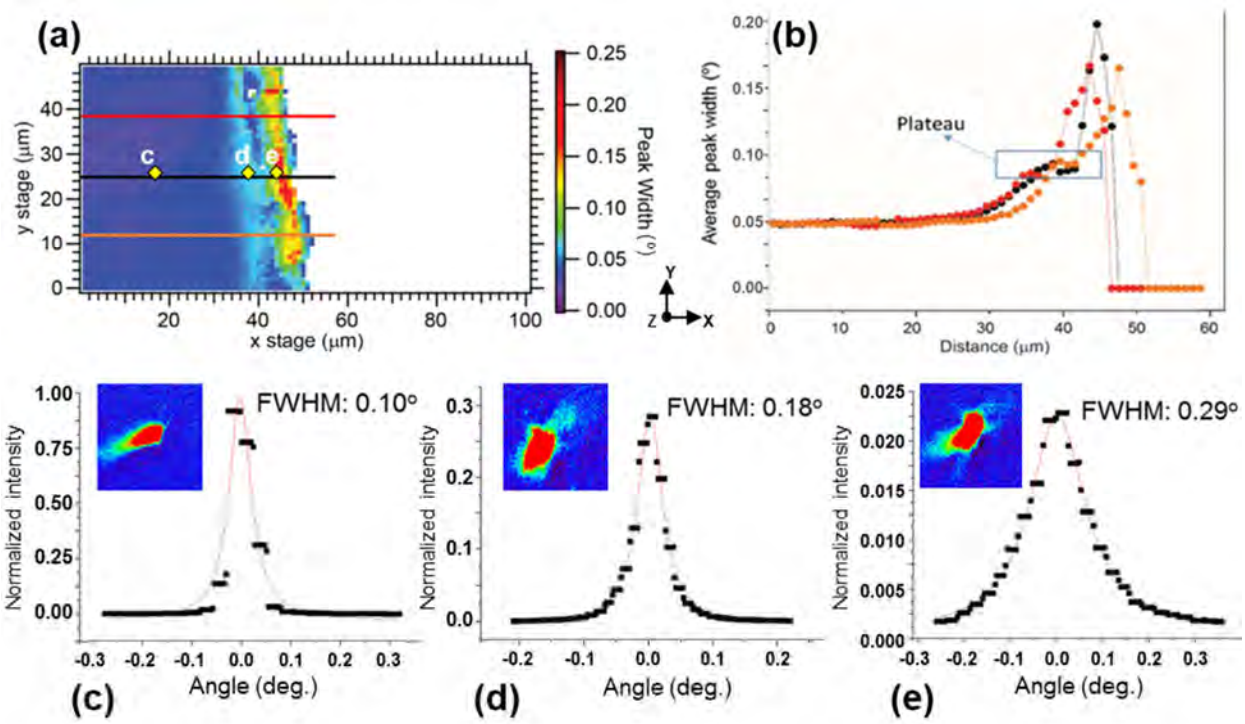

Figure 3. *(a) Average peak width distribution of the scanned area; (b) Average peak width evolution along the patterns (three lines parallel to the X-axis on Figure 3a); (c-e) Broadening of the* $(0\bar{1}3)$ *Laue peak width in three arbitrarily chosen spots corresponding to the yellow dots on Figure 3a: plotted in 2D projection along the most broadened direction (top), and in topographic projections (bottom). Peak width measured by fitting the intensity with Lorentzian distribution function.*

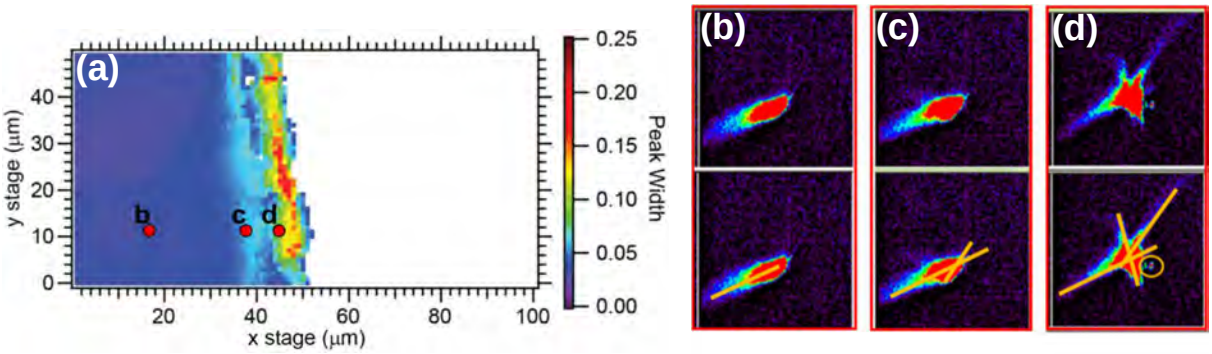

Figure 4. *(a) Average peak width distribution, and (b-d) Streaking of the* $(0\bar{1}3)$ *peak in more than one direction, as moving along the direction parallel to the X-axis, from the deep bulk towards the steel-oxide interface (corresponding to the spots* b - d*, respectively, labeled on fig. 4a). (b) Only one dislocation direction in deep bulk. (c) Increase of strain coincides with second dislocation direction and the beginning of peak broadening. (d) Large strain and peak width, with three directions of dislocation. Side peaks forming (circled spot on fig. 4d) indicate a new grain formation.*

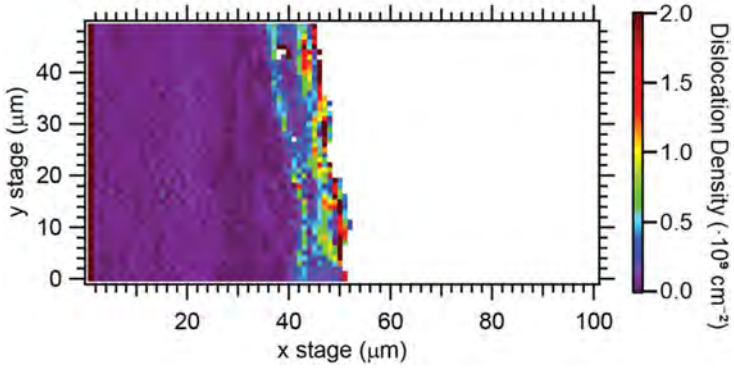

Figure 5. *Dislocation density map of the XRD-scanned area.*

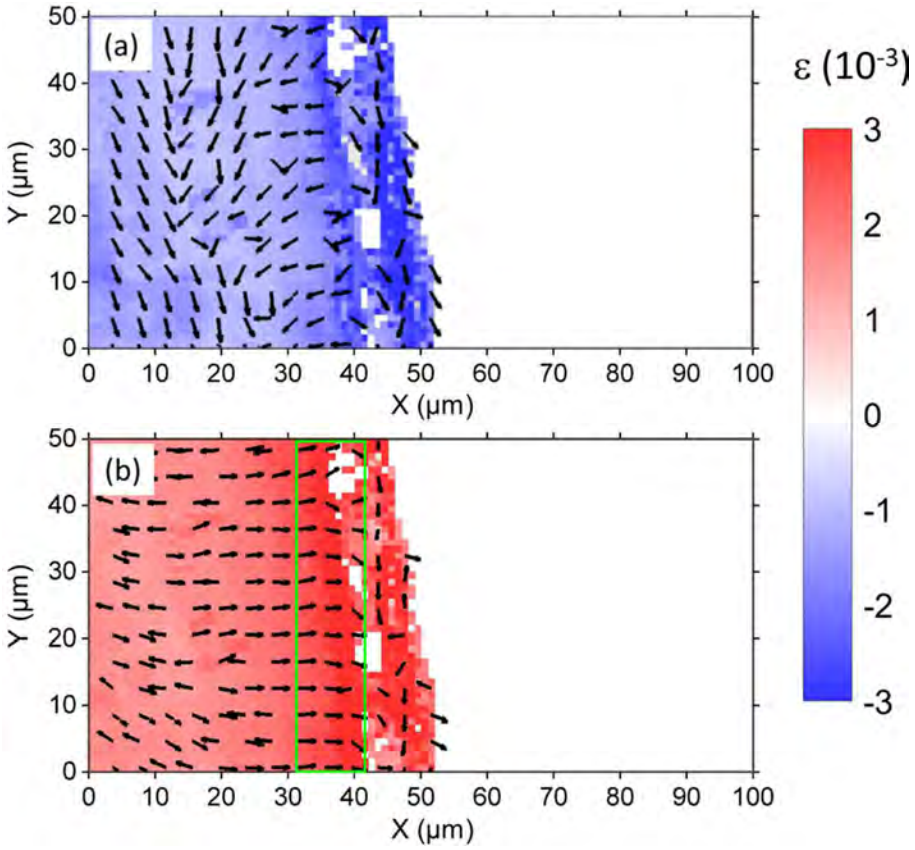

***Figure 6**. (a) Compressive principal strain and (b) tensile principal strain in bulk (next to the oxide scale). Projections of the principal strain axes on the X-Y plane are denoted by arrows in every third pixel. A zone in the bulk next to the steel-oxide interface suffers compression (due to both thermal expansion mismatch and internal oxidation), while below that zone there is a compensatory (reactive/consequent) tension maximum (green rectangle in Figure 6b).*

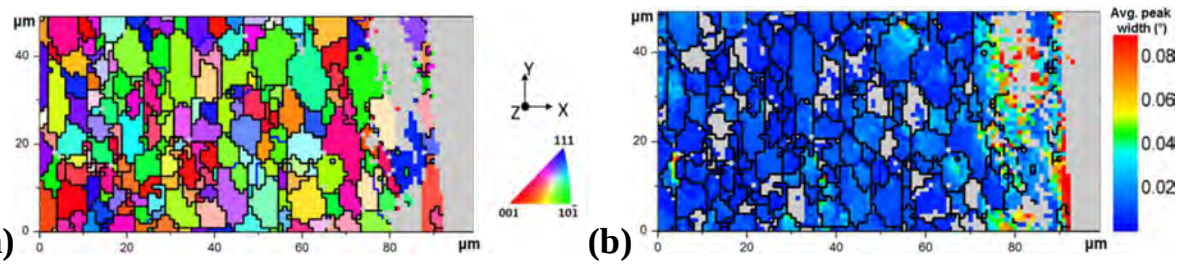

***Figure 7**. (a) In-plane orientation map in X-direction and (b) peak width distribution map of an ALK sample polished only but without treatment in LBE.*

GRAPHICAL ABSTRACT

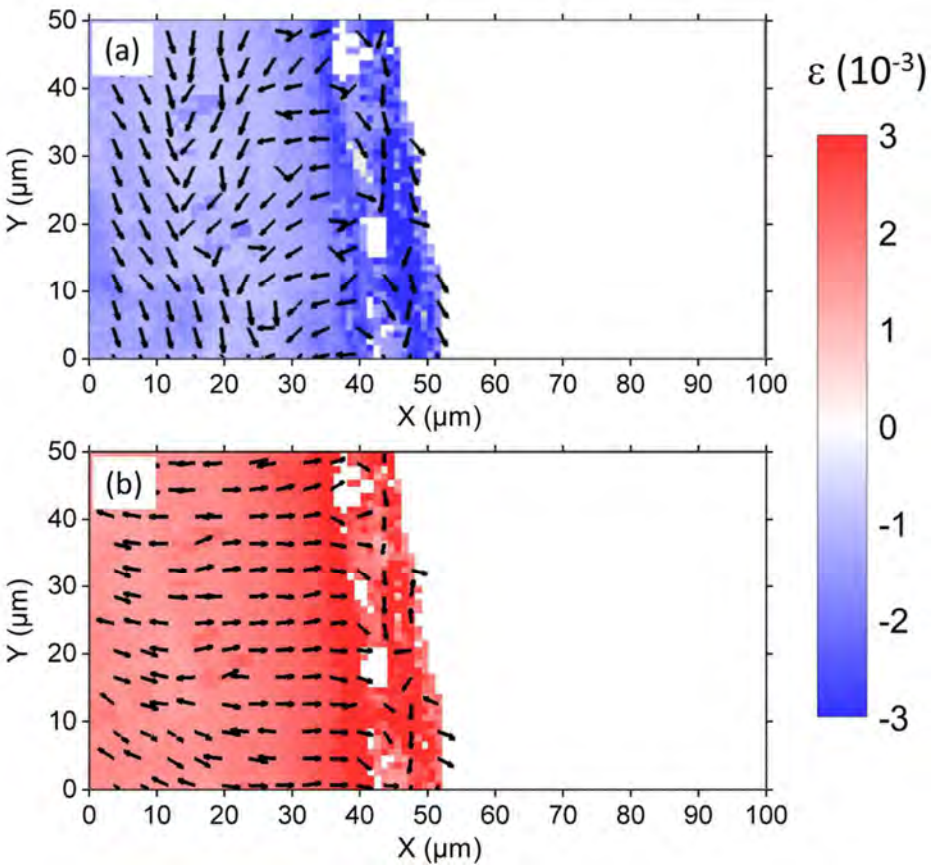

Compressive (top) and tensile (bottom) principal strain distribution in the μXRD-analyzed ferritic Fe-Cr-Al alloy material, in the bulk next to the alloy/oxide interface (arrows denote projections of the principal strain axes on X-Y plane).